Fibre geometries and their contribution to the global unidirectional tensile properties of enset fibre-reinforced epoxy composites.

ASHEBRE AREFE, Mengstu, GEBRESLASSIE, Mulualem Gebregiorgis <http://orcid.org/0000-0002-5509-5866> and WILLEM VAN VUURE, Aart

Published version

ASHEBRE AREFE, Mengstu, GEBRESLASSIE, Mulualem Gebregiorgis and WILLEM VAN VUURE, Aart (2024). Fibre geometries and their contribution to the global unidirectional tensile properties of enset fibre-reinforced epoxy composites. Composites Part A: Applied Science and Manufacturing, 185: 108294.

Fibre geometries and their contribution to the global unidirectional tensile properties of enset fibre-reinforced epoxy composites

Mengstu Ashebre Arefe[a,b], Mulualem G. Gebreslassie[b,c], Aart Willem Van Vuure[a]

[a]Department of Materials Engineering, KU Leuven, Kasteelpark Arenberg 44, 3001 Leuven, Belgium
[b]School of Mechanical and Industrial Engineering, Ethiopian Institute of Technology-Mekelle (EiT-M), Mekelle University, Mekelle, Ethiopia
[c]Materials and Engineering Research Institute, Sheffield Hallam University, Howard St. Sheffield, S1 1WB, UK

Abstract

This study investigated the potential forms of enset fibres and their tensile properties. Microscopic images of the fibre cross-section were collected, and image analysis was carried out in MATLAB. As a result, four distinct fibre shapes were identified and their likelihood of occurring as well as- their area contribution to the fibre bundle were determined. These fibres have distinct tensile strength, Young's modulus, and strain-to-failure values, distinguishing the strongest and weakest fibres. The strength distribution of these fibre shapes does not conform to the Weibull theory. However, it follows the scenario that fibres with the biggest perimeter-to-area ratio provide the weakest values and vice versa. This shows that the tensile properties of fibres are influenced not only by their material properties but also by their geometric shape. As a result, fibres of different shapes contribute differently to the global tensile properties of the fibre-polymer composites.

Keywords

Fibre Geometry, Morphologic Analysis, Tensile Properties, Load Contribution Model

1. Introduction

The increasing interest in using bio-based fibres as reinforcement in polymer composites is driven by their potential for low cost, biodegradability [1] and environmentally friendly attributes, including low energy consumption and minimal greenhouse gas emission during processing [2]. Lignocellulosic fibres, as lightweight and strong reinforcing elements in polymer matrix composites, offer good resistance to corrosion [3,4], fatigue and creep [5][6]. Moreover, the higher specific strength and elastic modulus of natural fibres, such as flax fibres in comparison to glass fibre, further enhance their potential use in structural applications [7].

The suitability of these fibres for specific applications is contingent upon the performance properties of the technical fibres. In bio-based fibres, 'technical fibres' refer to lengthy, thick fibres formed by

bundles of elementary fibres interconnected by pectin, primarily obtained through hackling and scutching. Unlike synthetic fibres, whose geometry can be shaped according to specific requirements using sizing dies, bio-based technical fibres possess complex shapes and morphological structures that naturally develop based on their intended function within the originating plant when it was alive [8]. This inherent quality enables bio-based fibres to exhibit diverse shapes. A survey of plant fibre morphology micrograph reports indicates that the shapes can vary from the kidney-type and oval shape appearances for sisal and palm phoenix fibres, respectively [9][10], to quasi-circular shapes for coir and hemp fibres [11] [12]. There are also complex microstructural appearances, such as flax fibre, that make it difficult to model their morphological appearance with the known geometries [13]. Furthermore, fibres from the same plant may have diverse geometric shapes in some circumstances.

Cognizant of the influence of other factors such as the age of the fibre source, the location of fibre extraction, the species of fibre sources [8,14–17] and other variables, on the mechanical performance of the bio-based technical fibres, the effect of fibre geometry is assumed to have considerable impact. Fibres with the same cross-sectional area but different shapes exhibit variations in fibre perimeter, significantly affecting the properties of the fibre-matrix interface. Study reports on glass and carbon fibre composites explained this phenomenon. Thomason's research [18] on the circularity of fibres in glass fibre composites revealed that flat and elliptical fibres have shorter critical lengths than circular fibres, leading to improved tensile strength in short fibre composites. Similarly, Kitagawa et al. [19], in their study of the effect of fibre shape on the compression properties, found that a composite reinforced with kidney-type fibres in carbon composite delays crack initiation and suppresses crack accumulation compared to circular fibre-reinforced composite. Moreover, Liu et al. [20] investigated the effect of triangular and circular carbon fibres on flexural properties and reported that triangular fibres performed higher flexural strength and flexural modulus compared to circular shapes. Therefore, in the case of synthetic fibres, non-circular fibre shapes exhibit superior interface properties, surface energy and good wettability compared to circular fibres, attributable to the increased surface area exposure in the fibre-polymer interface [21].

It is believed that the more complex the microstructural appearance, the greater the enhancement in the fibre-polymer interfaces. However, modelling complex shapes with the known geometry is

challenging. Thomason extended his work to establish a representative geometry for the complex geometric shapes of natural fibres such as coir, kenaf and jute fibres [22]. He developed an elliptical description of these fibres and differentiated the shapes based on the ratio of the minor to the major axis of the ellipse. Similar work was done by R. Ntenga and A. Beakou [23] to represent the morphologic variation of bio-based fibres. They conclude that while the cross-section area of sisal and palm fibres can satisfactorily be assessed by circles, the hemp, flax, and nettle fibres can be assessed by elliptical models. Despite efforts to study the importance of fibre shapes, these studies did not investigate the impact of fibre geometries on mechanical performance. Additionally, the studies have put limited options to model the cross-sectional area of the intricate shapes of the fibres, making it challenging to accurately represent fibres in the study and other remaining bio-based fibres with these known geometries. Consequently, modelling the microstructure and geometry of the bio-based fibres, crucial for offering fundamental support for designers and materials engineers to develop a predictable property based on the fibre microstructure [24], faces hindrances.

In summary, while there have been commendable efforts to explore the influence of fibre shapes on glass and carbon fibres, the exploration of natural fibre shapes remains an intriguing and open avenue for research. The consulted study reports on synthetic fibres predominately concentrate on elucidating the effect of fibre shapes on the properties of the fibre-matrix interface, with a noticeable gap in addressing their influence on the tensile properties. Based on the available information, the tensile analysis of natural fibres did not consider the complexity of their geometry and variations in shape from fibre to fibre. Additionally, the current parameters are insufficient to establish a relationship between the fibre's mechanical response and its geometric appearance. As a result, the question of how subtle geometric intricacies affect the mechanical properties of natural fibres is still unanswered in the scientific community. The existing models do not accurately represent the shape of fibres, making it difficult to model and characterise natural fibres based on their microstructure. Consequently, the influence of geometry on the tensile properties of natural fibres is an open question.

Therefore, this study focuses on investigating the shapes of enset fibre as well as their relations with tensile properties. Enset fibre is a long, low-density fibre derived from the enset plant stem (ensete ventricosum). The enset plant is distributed across the tropical belt, but it is only cultivated and prolific in Ethiopia [25], where it provides sustenance for about 15 million Ethiopians who live in the

highlands of Southern, Southwestern, and Central Ethiopia [26]. It is a perennial herbaceous plant that is mostly used for human and animal consumption [27]. The enset fibre is a byproduct of food extraction, and its length can reach up to 3 meters, depending on the length of the stem.
Based on our experience, a microscopic examination of the failure area of enset fibre reinforced composite samples under a tensile load showed varied fibre shapes with different failure phenomena. This variation in microstructural shape and distinct failure profile to the respective fibre shapes is reasonably a sign to advocate the influence of geometry on the tensile properties of the fibres. As a result, we formulated a hypothesis that illustrates "Geometric fibres show variable failure topography in the unidirectional tensile test due to differences in their strength and elastic modulus values, as well as differences in contribution to the applied tensile load". To validate the hypothesis, fibre geometries and their tensile properties were investigated.

2. Materials and Methods

2.1. Fibres

Enset fibres were collected from enset plants in Ethiopia's Wolisso district, Grugea zone. The fibres are obtained from local people in this study, and there is no control over the source plant's age, the position of the stem from which the fibres are extracted, and quality. However, a general process for extracting fibres from the enset plant can be established. Enset fibre is a by-product derived from the enset plant after the extraction of starch-rich food. It is a primitive method of extraction in which locals cut the stem of a plant that they believe is mature enough to give a significant yield. They disassemble it into layers and place each one on top of a flat piece of wood that is first installed at an elevation under an angle of around 60^{o}-70^{o}. The extraction is then carried out through decortication using dry sharpened bamboo.

The fibres were then stacked along their axis, and stiff cylindrical materials were inserted inside the bundles to keep the fibre straight and prevent bending or collapse during drying, transporting, and conserving. The fibres were cut into a manageable length of about 50cm, kept at the source for three months, and then stored for two months in the natural fibre conditioning room (21 ±2 ^{o}C and 50 RH) at the Department of Materials Engineering, KU Leuven.

2.2. Impregnated fibre bundle samples

Fibres were dried at 60°C for 24 hours to eliminate moisture and determine dry weight. Impregnated fibre bundle test (IFBT) samples were prepared following the method illustrated by Bensadoun [28] using epoxy as an embedding matrix, cured at 70°C for an hour, and then consolidated at 150°C for another hour in a temperature-controlled manual press machine. Four samples of size 250 mm x 10 mm x 2 mm were produced (Fig.1). A small rectangular section of size 20*10*2 mm^3 was cut from each IFBT sample for microstructural investigation.

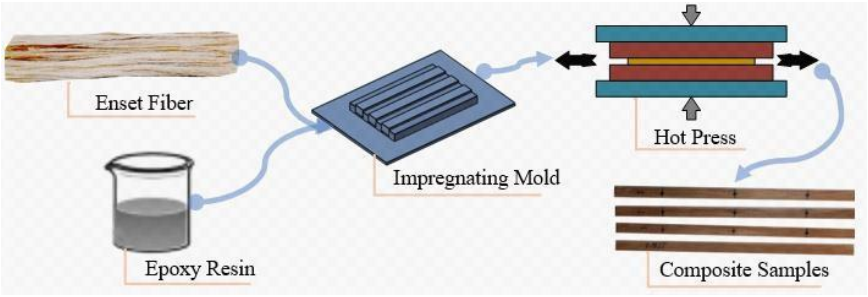

Fig. 1. Enset fibre reinforced composite IFBT samples production.

2.3. Fibre shape investigation

The microstructural study reveals significant details about the fibres' geometric appearance, cross-sectional area, perimeter, approximate diameter, and other characteristics. To investigate the microstructural features of the fibre, rectangular samples were placed in a typical cylindrical polyethene cup with a diameter of 25 mm and a height of 15 mm (Fig. 2a), which was then filled with epoxy resin and degassed for 10 minutes to remove any air bubbles. Curing was carried out inside a desiccator at room temperature for 24 hours.

The samples were ground in the Metallographic Specimen Grinding and Polishing Machine, METAPOL 260, with different grades of silicone carbide sandpapers, followed by polishing with 1200 and 4000 grit polishing paper to achieve a surface finish of 6 microns. The polishing work continued with magnetic plates using 3µm and then 1µm diamond suspensions. This polishing was done on a semi-automated polishing machine, Struers LaboForce-100, with both the spindle and the worktable rotating at a speed of 150 revolutions per minute in the same rotational direction. A minimal load of 15N and 10N was alternatively applied to avoid damage to the natural fibres during polishing and to promote an appreciable view of the fibre microstructure. Further polishing of

samples was done on the same machine using OPS (Oxide Polishing Suspensions) (active oxide polishing fluids) with a foam-like magnetic polishing plate to obtain clearer microstructural images. A surface roughness of below 1 micro is obtained as a result of these fine polishing techniques and polished samples were maintained inside a soft tissue to avoid any damage to the surface.

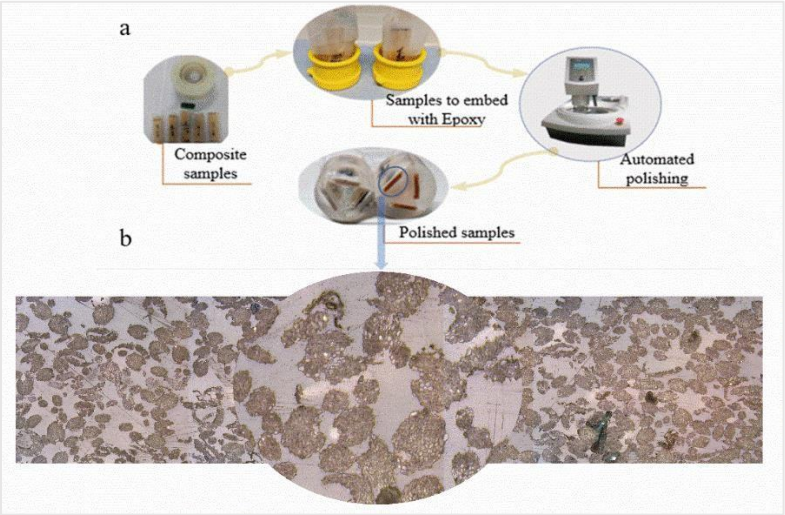

Fig. 2. a) Sample preparation procedure; b) microscopic image of enset fibre-reinforced composite

Microstructural images were captured using a stitched scanning mode on a confocal microscope with a magnification level of 10X. Four images were collected using the confocal microscope (Sensofar-Neox) for geometric analysis of the fibres: an inference microscopic image is displayed in Fig 2b.

2.4. Probability of occurrence and areal contribution

Following sample imaging, the technical fibres were grouped based on their shapes based on visual observation of the microstructural images. First, fibre-shape families are proposed by using existing shape descriptors described in numerous studies, such as the elliptical fitting based on the ratio of large to small diameters by Thomason [22] and the parametric equation for kidney-shaped fibres by Kitagawa [19]. Additional geometric indicators were evaluated based on the concavity and convexity of the fibre boundaries and their position. The assignment of individual fibres to the proposed fibre shape families was based on geometric similarity. Initiating an elliptical approach to the technical fibres helps to identify the individual fibres more easily. To depict the morphological appearance of the different fibre shapes, a generic approximation equation was implemented.

Four microscopic pictures holding 1822 technical fibres were considered to calculate the probability of occurrence and areal contribution of defined fibre geometries. The region Analyzer application tool in MATLAB was used to generate statistical data on these fibres, such as their cross-sectional area, perimeter, and equivalent diameter. The likelihood of occurrence was figured out by assigning a geometric code to each fibre category and filtering these codes was done in Excel. To measure the fibre areal contribution of each type, the area of each fibre geometry was extracted simultaneously with the geometric code. This geometric classification of the enset fibres helps to further characterize these fibres about their tensile properties and their contribution to the global enset reinforced polymer composite properties.

2.5. Tensile properties of the fibres of different geometry

Tensile tests were performed on the geometrically recognized fibres to explore the tensile performance of the respective technical fibres. For fibre selection and single fibre tensile testing, enset fibres with a total length of 310 mm were prepared and cut into sections of 60, 150 and 100 mm respectively for the various procedures described below. Two steps were involved in the selection of individual fibres based on their geometric shapes. The first stage is pre-screening where fibres are cut into an approximate length of 60 mm and embedded with a viscous substance that can keep the fibre straight and let it adhere to the worktable of an optical microscope during geometric shape inspection. The embedded part of the fibres was carefully cut using a scissor and transferred to an optical microscope to examine the fibre geometry (Fig. 3a). This straightforward method provided an approximation of the fibre geometry during fibre preparation.

Because the above procedure does not provide the correct fibre shape, a second examination was conducted to find the right shape of the fibres. This step determines the microscopic nature and appearance of the fibre. To maximize the likelihood of receiving a decent image from the single fibre polishing, a 150mm long fibre was prepared and cut into five pieces, taped together, and placed in a narrow Polyethylene pipe. The fibre holding pipe was secured in a supporting fixture to keep them vertical when embedding the fibres with epoxy resin in a standard cylindrical cup as described in section 2.2.2, (and see also Fig. 3c). The resin was degassed and cured at room temperature in a desiccator. After polished embedded samples were obtained using automated polishing equipment, the geometry of each fibre was examined using an optical microscope at high

magnification power, X50.

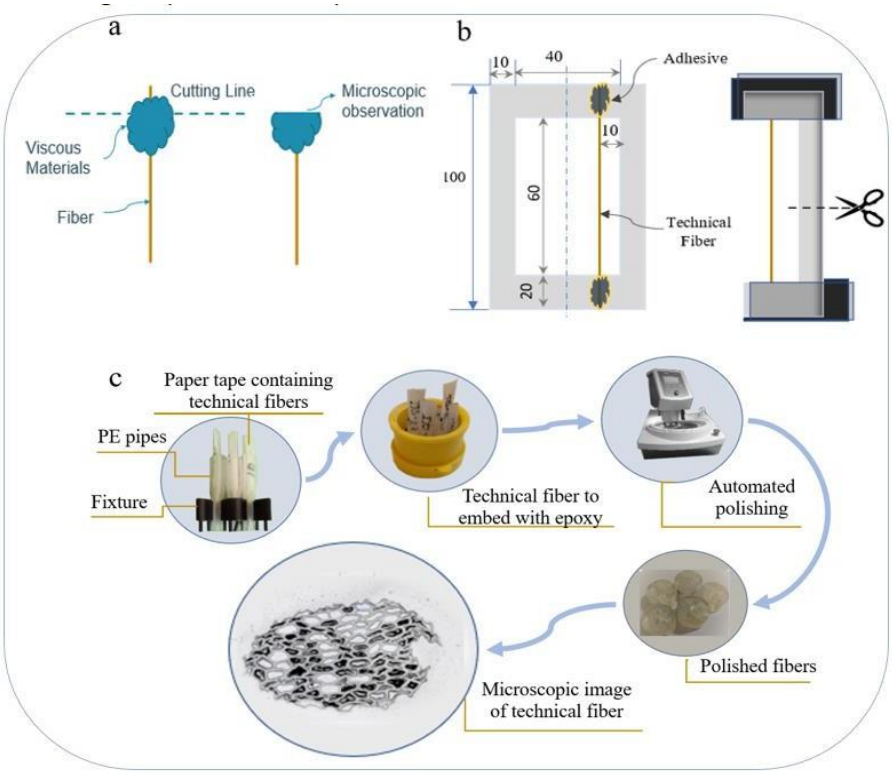

Fig. 3. Fibre preparation for tensile testing and techniques of selecting fibres based on the geometric appearance for the tensile test; a) simple fibre selection technique, b) fibre preparation for tensile testing, c) technical fibre polishing process for micrograph-based fibre selection.

To explore the tensile behaviour of the various shaped fibres, a tensile test was performed on the technical fibres. Fibres of 100 mm in length were prepared and dried in an oven at 60°C for 24 hours, and their dry weight was used to calculate the fibre's cross-sectional area, with the density of the fibre being 0.94 g/cc (lower density due to large contribution of the lumen). About 20 technical fibres were prepared in the same procedure for each geometry category and then placed in a humidity-controlled conditioning box with a saturated magnesium nitrate solution for seven days at room temperature, to equilibrate at 50% RH.

Sample holders were prepared from white paper for proper straightness and alignment of the fibres and to provide proper support during clamping with the machine grips. Papers were cut into a rectangular form with an overall dimension of 60 mm X 100mm and further partitioned to provide a gauge length of 60mm (Fig. 3b). The fibres were attached to the sample holder first with a tiny paper tape to easily control their alignment and then firmly adhered with cyanoacrylate

adhesive. After air-drying the adhesive for three hours, the fibre holding papers were folded and inserted into the machine grips, positioned properly and the vertical side of the paper sample holder parallel to the fibre axis was cut. The tensile test was performed using an Instron 5943 with a 100N load cell and a 1mm/min tensile speed. Sample strain was calculated from the displacement of the machine, which will give some underestimation of the fibre modulus. Single fibre tests in this fashion serve to obtain an understanding of the fibre strength distribution (see next section – Weibull analysis).

To also obtain accurate data on fibre modulus and to understand the transfer of properties to the composite, impregnated fibre bundle tensile tests were performed on eight enset fibre reinforced epoxy matrix composites with an average fibre volume fraction of 48 % to investigate the contribution of fibres of defined geometric shapes to the global tensile properties of the fibre composite and to study composite failure modes. Samples were first placed for 24 days in a closed glass box containing a magnesium nitrate saturated solution that maintains humidity of 50% RH at 21 ± 2°C [29]. A tensile test was performed on samples according to ASTM D 3039/D 3039M using an Instron 5567 with a load cell of 30 kN at a speed of 2mm/min. An extensometer was used to record the strain value. The tensile characteristics of the fibres were back calculated using the rule of mixtures established by Eq. 1 and Eq. 2.

$$\sigma_f = \frac{\sigma_c - \sigma_m(1-V_f)}{V_f} \quad (1)$$

$$E_f = \frac{E_c - E_m(1-V_f)}{V_f} \quad (2)$$

2.6. Two-parameters Weibull statistics of failure prediction

Weibull's theory is based on the weakest link concept, which accurately describes observed component failures [30] when the failure is directly tied to the material's fragility [31]. This fragile section appears in natural fibres due to a weak link on the central lamella or a smaller diameter part [32]. When fibres are brittle and tensile strength is determined by faults, this distribution function aids in describing their tensile qualities [[33]. The Weibull distribution with two parameters is a widely used method for describing the stress distribution of natural fibres. According to the Weibull statistics, the likelihood of failure is given in Eq. 3.

$$F(\sigma) = 1 - \exp\left(\frac{\sigma}{\sigma_0}\right)^m \quad (3)$$

Where F(σ) is the probability of failure of the fibre at stress level less than or equal to σ. m is the Weibull modulus often called the form or shape factor since it defines the width of the distribution function. σ_0 is the characteristic strength or scale factor. This scales the stress (σ) corresponding to the failure stress of the fibre. Weibull statistical analysis has been applied in reinforcing fibres with the assumption that the materials do not show plastic deformation before breaking and that the failure is due to flaws. Weibull analysis has been applied to the characterization of tensile properties of flax fibre, bamboo fibre, agave fibre [32][34] [35], carbon fibre [31] and glass fibre [36]. The probability of failure of each sample, F (σ), is found Bernard's estimator [37]. To estimate this value, the tested samples are arranged in ascending order based on their strength and then Eq. (4) is applied.

$$F(\sigma) = \frac{n-0.3}{N+0.4} \quad (4)$$

Where N is the total sample size and n is the n^{th} ranked sample. Rearranging Eq. (3) and applying a natural logarithmic function to obtain a linear relationship provides Eq. (5).

$$ln\left(ln\left(\frac{1}{1-F(\sigma)}\right)\right) = m\,ln(\sigma) - m\,ln(\sigma_0) \quad (5)$$

The constant parameters of the Weibull distribution, m and σ_0, are obtained from the Weibull diagram, a curve of $ln\left(ln\left(\frac{1}{1-F(\sigma)}\right)\right)$ as a function of $ln(\sigma)$. The value of the characteristic strength is calculated by equating $ln\left(ln\left(\frac{1}{1-F(\sigma)}\right)\right) = 0$

While this method has been widely used to investigate the effect of length/volume on tensile strength, we use Weibull statistics to predict the scattering of fibre strength among fibres of different geometry and demonstrate the applicability of Weibull theory based on the volume of the fibres due to changes in diameter.

2.7. The global contribution of the fibres

The tensile properties of the composite fibre were investigated by creating a stress-strain map for all types of fibres. The average strength and strain-to-failure values are used to create this map. The stress contribution of all fibre types was next evaluated, considering the fibres' areal contribution, the stress-strain curve's slope, and the strain-to-failure value of the fibre in question. The back-

calculated fibre strength is used to identify the fibre that determines the overall failure of the composite.

The microstructural failure areas of the fibres of the IFBT samples were examined under a scanning electron microscope (SEM). The defective areas were coated with platinum and analysed using Philips equipment (Eindhoven, Netherlands). The failure phenomena of the individual fibres, which represent different fibre shapes, were investigated by taking topographical micrographs of the failure area.

3. Results and Discussion

3.1. Enhancement and post-processing of microstructural images

The morphological structure of the enset fibre is illustrated in Fig. 4. The technical fibres of enset exhibit diverse fibre geometries, ranging from round to complex shapes (Fig. 4a). Moreover, there is a notable variation in fibre size within the fibre bundles. These observations underscore that fibres originating from the same plant can have different shapes and morphological appearances. Additionally, enset fibres contain large-size lumens, the hallow component in elementary fibres, making a substantial contribution to the fibre's cross-sectional area, resulting in the fibre being porous and lightweight (Fig.4b).

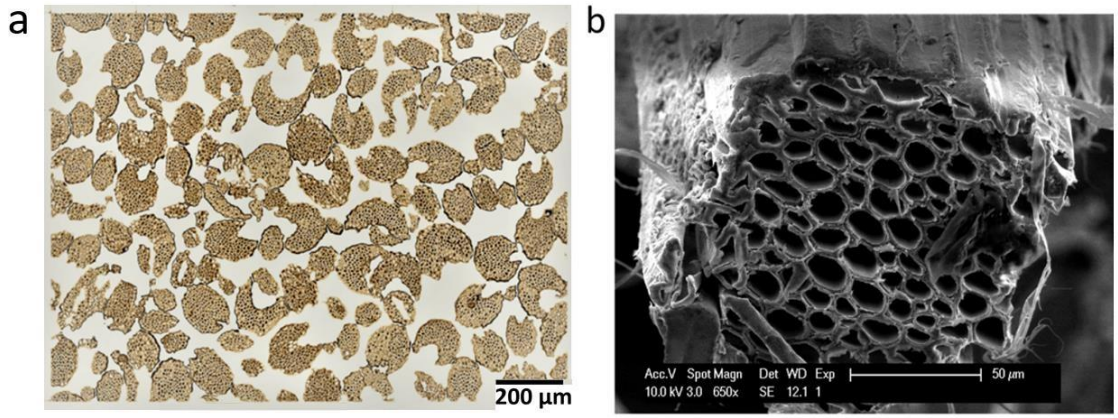

Fig. 4. Enset fibres; a) micrograph of microstructural appearance of enset technical fibres and b) SEM of technical fibre morphology.

To analyze the fibre shapes, their probability of occurrence, and their areal contribution to the fibre bundles, four large size colour images were collected from a confocal microscope with a magnification power of 10x with stitching scanning mode. An interactive application of MATLAB

and GIMP was used to perform image improvement and post-processing. The microstructural image (Fig. 2b) was recalled in MATLAB and the colour intensity difference between the foreground (fibre) and background (matrix) was first determined using the MATLAB program code. It has been noticed that the colour difference result does not indicate a distinct segmentation (Fig. 5a) caused by the modest density differences between the fibre and the matrix, as well as the fibre's significant lumen contribution which creates voids inside the fibre.

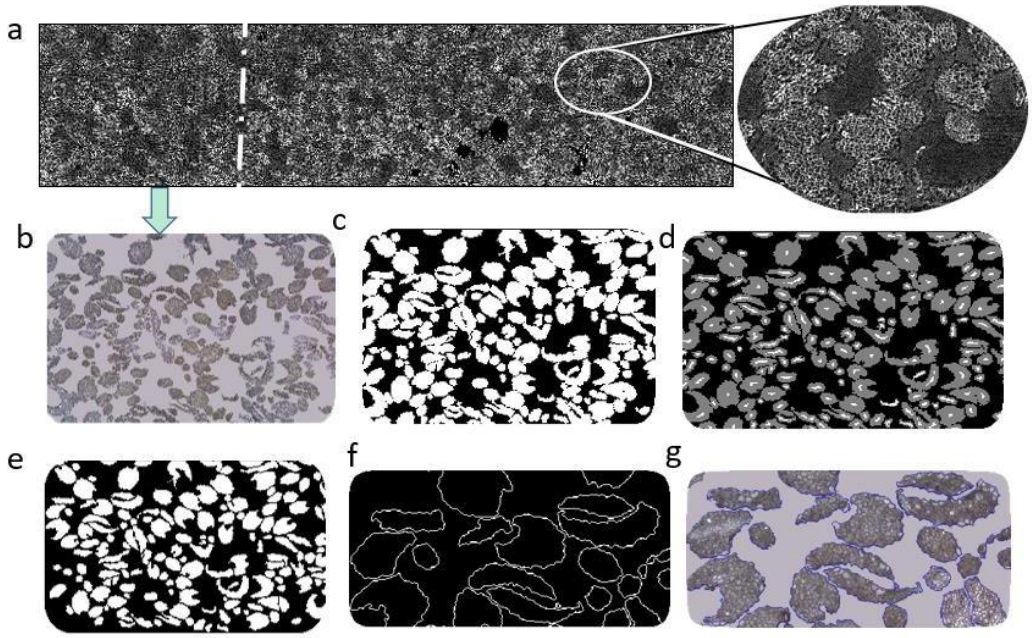

Fig. 5. Microscopic image enhancing and post-processing to segment and extract the fibre images; a) fibre-matrix colour intensity test, b) GIMP supported image segmentation, c) colour-based fibre image extraction and binarization, d) segmentation and contact region separation, e) post-processed microscopic image of the fibre, f) extracting the edge of the fibres with the morphologic operation, g) validation of the post-processed image of the fibres with the original microscopic image.

As a solution, GIMP was used to achieve foreground and background segmentation as well as noise removal (Fig. 5 b). Colour-based image extraction has been developed to produce visible fibre geometry that at the very least preserves each fibre's boundary (Fig. 5c). GIMP has also been used to aid MATLAB during distance transformation to distinguish contact zones of two or more fibres depending on the fibres' correct geometric appearance. The post-processed fibre shape (Fig. 5d) has been constructed, confirming that the segmentation and distance transformation contact

separation is correctly addressed. The validity of the post-processed image is confirmed by first creating the fibre edge (Fig. 5e) and then overlaying these edges on the initial microscopic image (Fig. 5f). It is proved that the edge formed after multistep morphological processes fitted the original microstructural image accurately. For the remaining three microscopic images, the step-by-step interactive microscopic image analysis using MATLAB and GIMP was continued until the morphological process provided an acceptable fibre geometry that duplicated the original microscopic image.

3.2. Fibre shapes and geometric modelling

To identify the shapes of the enset fibre, a detailed visual inspection of the microstructural images was performed. This was done with Region Analyzer, a MATLAB application tool that displays a distinct colour when using the generated picture number. This ensures that all fibres in the huge confocal microscope image are considered. Since enset fibres have different shapes (the reader can refer to Fig. 4 a, and Fig. 5), current representative models in the fibre shapes were examined, and the various shapes of the fibres were surveyed to draw potential geometric representatives of the fibres [18,19,23,38]. As a result, four major fibre geometric shape groups were established, and individual fibres were categorized according to their appearance in the designated geometries. Four major geometric shapes were recognized and named because of their appearance: half-moon shape (HMS), circular/oval shape (COS), elongated shapes (EOS), and intricate shapes (ITS). Fig. 6 shows the fibres' morphologic structure, with an approximated representative size generated from known geometric shapes and compared to their true size. The geometric boundaries of the HMS fibres are formed by curved lines of concave and convex forms that are smoothened at their intersection point (Fig. 6a). This type of architecture provides a half-moon or a kidney-type shape. On the other hand, COS fibres are characterized by two convex curves (Fig. 6b). Elongated fibres have straight or arc cylindrical slots along their cross-section (Fig. 6c). Fibres with an intricated shape that cannot be categorized into one of the three geometrically defined fibre shapes are grouped under ITS (Fig. 6d). Furthermore, fibres that cannot be classified into one of the four forms above due to their size are grouped and referred to as small shape (SMS) fibres (Fig. 6e). Those fibres have a similar shape as COS fibres, but they are small due to a few numbers of elementary fibres and there is no reasonable instantaneous size transition to associate them with circular

shaped fibres.

To model the various shapes of enset fibres, the parametric equation used in the Kitagawa et al. study to depict kidney-type fibres, Eq. (6), was further modified. Additional parametric variables were introduced to enhance its generality, making it more applicable to the diverse contours of these fibres.

$$x(r_1,\theta) = r_1 * cost\theta + k_1 * e^{(-acos\theta - a)};\ y(r_2,\theta) = r_2 * sin\theta \quad (6)$$

Where r_1 and r_2 are the radius to the minor and major diameters of an ellipse, K_1 is the maximum distance from the convex curve to the ellipse curve in the direction of the major diameter. θ and a, in their order are the rotation angle from 0-2π to produce a complete loop and the shaping variable that controls the concavity and convexity of the curves at the fibre boundaries.

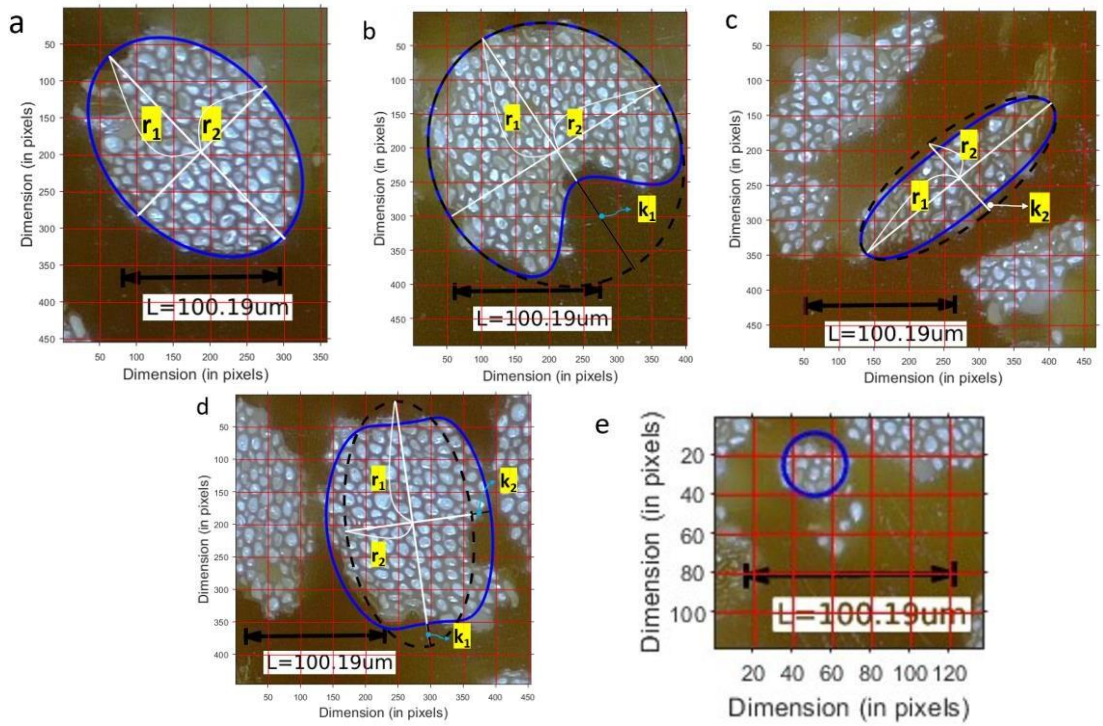

Fig. 6. Various geometric shapes of enset fibre are categorized based on their appearance; a) the half-moon shape fibres represented by convex and concave curves, b) the Circular/oval shape fibres represented by an ellipse or oval curves, c) the Elongated fibres described by arc slots, d) the intricate shape fibres and e) the small size fibres mostly represented by circular geometry.

The generic modelling equation (Eq. 7) allows for initiating approximation of the shapes using an elliptical fitting, as illustrated by the black broken lines in Fig. 6. In cases where the ellipse does not

accurately represent the fibre shape, the shape control variables are subsequently modified. This adjustment is made to eliminate some parts of the elliptical curve and accurately portray the edges of the fibre.

$$x = r_1 cos\theta \pm k_1(e^{(-acos\theta - a)} - e^{(acos\theta - a)});\ y = r_1 sin\theta \pm k_2(e^{(-bsin\theta - b)} - e^{(bsin\theta - b)}) \quad (7)$$

Where k_2 and b have similar function as k_1 and a, respectively, in the minor diameter direction.

The first terms in the generic equation, $x = r_1 cos\theta$ and $y = r_1 sin\theta$, provide an elliptical profile; forming a circle when a and b are equal. This allows modelling fibre shapes like COS fibres using elliptical shapes. Conversely, shapes such as HMS, EOS, and ITS shapes cannot be accurately modelled using elliptical fitting due to the presence of both concave and convex shapes at the fibre boundaries, resulting in irregular shapes. Hence, the components of the parametric equation $\pm k_1(e^{(-acos\theta - a)} - e^{(acos\theta - a)})$ and $\pm k_2(e^{(-bsin\theta - b)} - e^{(bsin\theta - b)})$, are utilized to control the shape on both sides of the minor and major axes. To model the shape of HMS fibres, Eq. (6) is used to manipulate the convex shape on one edge, deviating from the elliptical fitting. Similarly, the ITS and EOS fibres, can be represented by Eq. (7)

The initiation of an approximation to various enset fibre shapes through elliptical fitting facilitates the determination of major and minor diameters, encapsulating these shapes. Robust image processing tools like MATLAB have the capability to automate and generate these statistical values. Fig. 7 visually represents the minor and major diameters across different fibre geometry categories. Notably, the disparity between the major and minor diameters of EOS and ITS fibres is substantially higher than that of COS and HMS fibres. These differences carry implications for categorizing fibres based on their shapes.

Furthermore, these dimensions are instrumental to determine r_1 and r_2 to model COS fibre, r_2 to model HMS fibre and r_1 to model EOS fibre without the need of any shape control variable. In other words, the minor and major diameter of COS fibres, the width of HMS fibres, $2r_2$, and the length of the EOS fibres, $2r_1$, can be obtained directly from the elliptical approximation. However, to figure out the thickness of the HMS fibres , $2r_1$-k_1, the width of the EOS fibres, $2(r_2-k_2)$, and both the width and thickness of the ITS fibres, $2(r_1-k_1)$ and $2(r_2-k_2)$, respectively, can only be obtained through optimizing the shape control variables. For the representative images (Fig. 6) of fibre shapes, the parametric variables of the generic modelling equation are listed in Table 1.

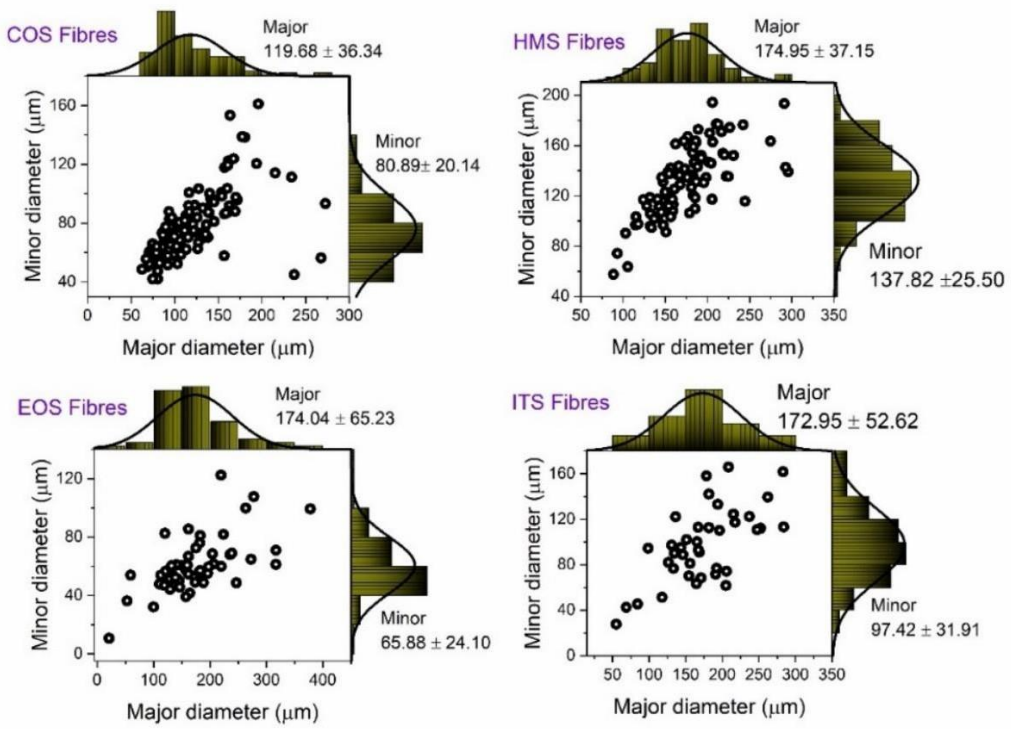

Fig. 7: The major and minor diameters of elliptical fitting to various fibre shapes in which the values of r_1 and r_2 are figured out.

Table 1

The values of the parametric equation fitting the various enset fibre shapes.

	Ellipse Parameters		Shape Control Variables			
Fibre shape	r_1 (μm)	r_2 (μm)	k_1 (μm)	k_2 (μm)	a	b
COS Fibre	156.8	111.1	0	0	0	0
HMS /Fibre	186.7	141.2	70.6	0	8	0
EOS Fibre	266.9	62.3	0	7.4	0	6
ITS Fibre	176.10	89.56	16.78	13.52	8	2

3.3. Probability of occurrence and areal contribution

Counting the number of fibres for each fibre family from post-processed microstructural images was used to find the probability of occurrence of fibres based on their shapes. The differently shaped fibres' likelihood of occurrence has been given as a percentage. The SMS fibres are the most common in the fibre population, followed by the HMS fibres (Fig. 8a). The ITS fibres' chance of occurrence is the lowest on record. These shape fibres are distributed randomly in the fibre bundle, as illustrated in the post processed images in Fig. 7, which is strongly connected to the likelihood of fibre occurrence [39].

The contribution of the fibres of different geometry to the area of technical fibre bundles has been characterized. Fig. 8b shows the area contribution of the fibres depending on their geometric appearance. This is the fibres' contribution to the cross-sectional area of the fibre bundle, reflecting their relative share of the imposed global tensile load. HMS fibres play a significant role in the tensile area, while COS fibres come in second.

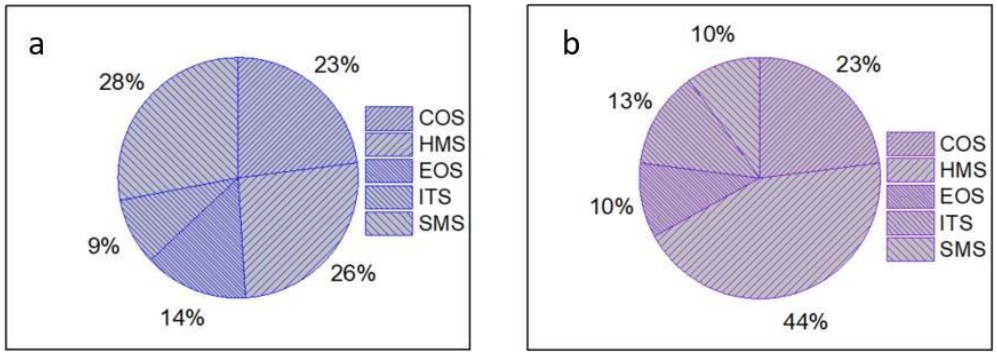

Fig. 8. Contribution of fibres of different geometry in the global fibre population: a) probability of occurrence and b) areal contribution of the fibres in the cross-section of fibre bundle.

The probability of occurrence and areal contribution of the different fibre types showed values which are not consistent. This is due to the fibres' relative average size. The areal contribution of HMS fibres is shown to be greater than their probability of occurrence. This shows that the average size of these fibres is the greatest. ITS fibres follow a similar pattern, but with a lower gradient than HMS fibres (areal share (%) to the probability of occurrence (%) ratio), showing that they are the second largest. Although SMS fibres are abundant, their areal contribution is the least, implying that these fibres are relatively small in comparison to the other categories of fibre. As a result of these two percentage graphs, it is reasonable to conclude that the average size of the different fibre types can be sorted out in descending order as follows: HMS – ITS –COS – EOS – SMS.

3.4. Tensile properties of fibres of different geometry

Fig. 9 shows the tensile properties of technical fibres based on their shape category. The tensile strength, Young's modulus, and strain-to-failure values of the various geometric shapes are found to differ substantially. COS fibres show superior performance in terms of tensile strength, 535.4 ± 1432.6 MPa, and Young's modulus, 30.8 ± 8.2 GPa, while HMS fibres are second, lower by 16.1% and 11.6%, in strength and Yong's modulus, respectively, when compared to COS fibres. (Fig. 9a and b). Fibres with intricate shapes show appreciable tensile properties when compared to HMS fibres.

Comparing with COS fibres, the EOS fibres show a low value in strength and Young's modulus but a high strain to failure; 33% lower in strength and 51% lower in Young's modulus but 32% higher in strain to failure (which is 2.5 ± 1.3%). The standard deviation of the strain to failure of EOS fibre is substantially higher, related to the fact that the tensile strength and Young's modulus of these fibres are very distributed. The HMS fibres, on the other hand, show consistent tensile properties and are predictable in their strength and strain to failure.

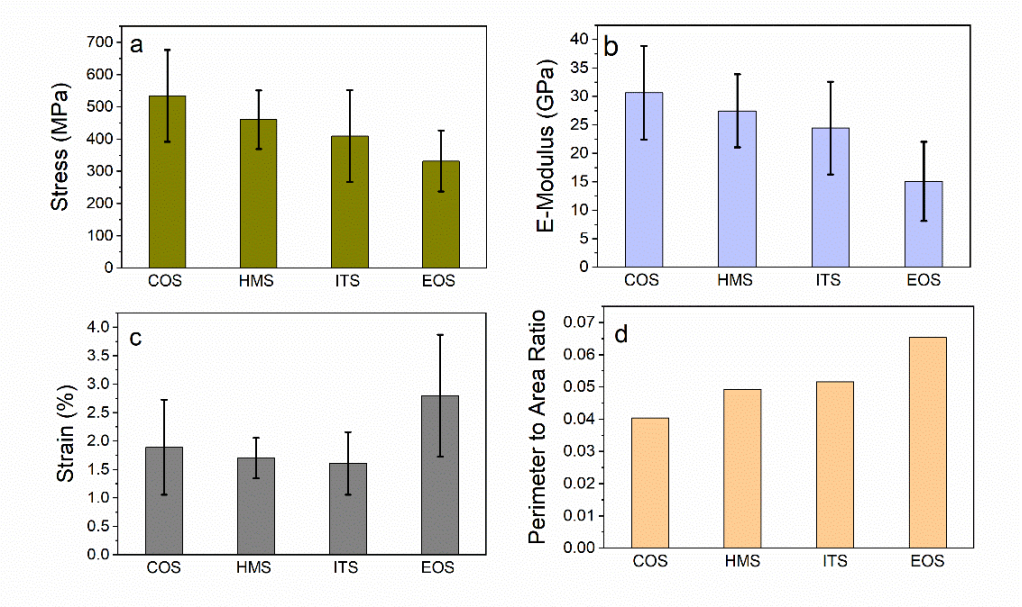

Fig. 9. Tensile properties of single fibre test a) tensile strength, b) Young's modulus and c) strain to failure of enset fibres of different shapes and d) their perimeter to area ratio. (Please note that these values refer to the fibres as they appear in the plant, with a relatively large lumen size and low density.)

There are big variations in the tensile properties of the technical fibres for all fibre forms. This is because single fibre tests are prone to scattered results due to high possible damage during extraction, preservation and test preparation [28] [40,41]. Additionally, the 20 fibre samples provided per category may contribute to the observed variation, as a larger sample size would likely result in less variation [28][42].

In the enset fibre geometric analysis, we have not studied the influence of fibre age on geometric appearance, shape transformation, and more importantly tensile qualities. Regardless of these factors, in this investigation, we noticed a consistently reasonable effect of fibre shapes on tensile

properties. The fibre shapes, which are characterized in terms of perimeter-to-area ratio, have brought every fibre shape category to experience a distinct tensile property. The perimeter-to-area ratio of the fibres in ascending order can be plotted as COS – HMS – ITS - EOS fibres as illustrated in Fig. 9d, which agrees with the statistical report in Fig.7. This is the reverse order for fibre tensile properties (both tensile strength and Young's modulus).

The tensile property values indicate that exposure to large boundary areas affects the stress fields during tensile stress development and reduces the magnitude of the stress uptake. This is a crucial observation because technical fibres are influenced not only by their material properties but also by their geometry. The boundary curve of the fibres is governed by the elementary fibres at the periphery, (Fig, 10a). These elementary fibres are intertwined through their central lamella and the interactions are mainly based on Vander Waal's forces [43] due to dipole-dipole interactions due to the variation in the functional groups. This means that elementary fibres located at the boundary, (Fig. 10b), are partly free on one side and partly entangled with the neighbouring elementary fibres inside the technical fibres (Fig. 10c). This likely results in the elementary fibres at the boundary and inside the technical fibres showing a different deformation behaviour as a response to the tensile load [44]. Because of the difference in traction and the generated Coulombic friction on the inside and outside sections, the elementary fibres at the boundary experience asymmetric stress when a tensile force is applied to the technical fibre. In such a loading scenario, it is conceivable to approach the concept of load-free extension as explained by [45]. When this notion is applied to the elementary fibres within the technical fibre, it results that the elementary fibres on the periphery have a comparatively load-free strain, implying that they contribute less to the absorption of stress. Therefore, compared to the elementary fibres in the inter part of the technical fibre, outer-surface elementary fibres experience lower tensile stress and contribute less to the overall Young's modulus during the iso-strain tensile loading. This leads to lower tensile properties of the technical fibres with a large perimeter to cross-sectional area ratio. The COS fibres have demonstrated high strength values and other geometric fibres follow in the order of their perimeter-to-area ratio (the higher the ratio the lower the strength). The sensitivity of fibre strength and elastic modulus to the circumference-to-area ratio is particularly observed in EOS fibres. In response to the high perimeter to area ratio, there is a counter decrease in tensile strength and elastic modulus.

In general, the tensile strength and Young's modulus of technical fibre are influenced by fibre geometry. Change in fibre shape leads to a change in the ratio of asymmetric loading to symmetric loading elementary fibres. However, the relationship between strain to failure and technical fibre geometric shape is inconclusive.

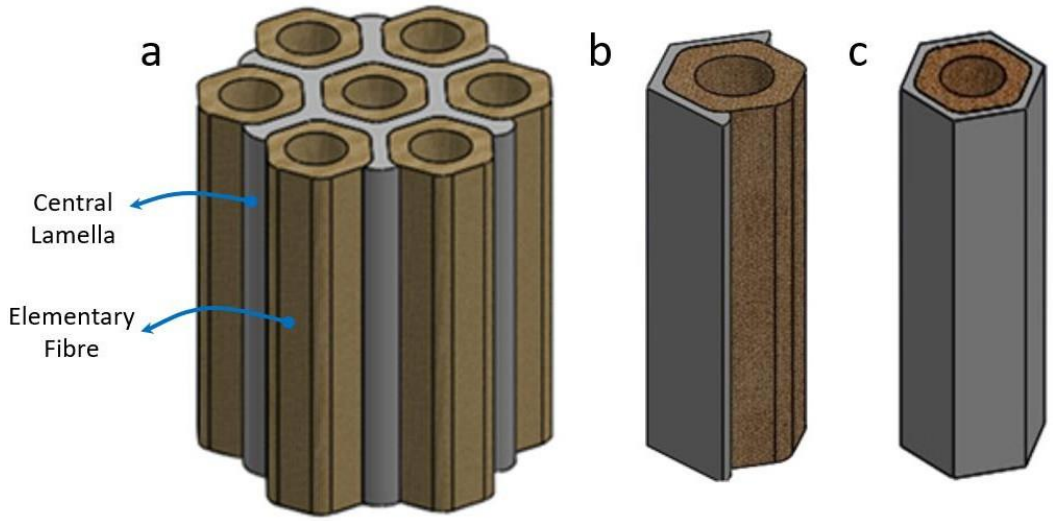

Fig. 10. Schematic illustration of the a) technical fibre arrangement, b) elementary fibre at the boundary subjected to asymmetric loading due to not fully enclosed by the central lamella and c) fully enclosed elementary fibre inside the technical fibre subjected to relatively symmetric loading.

3.5. The Weibull distribution of the tensile strength

The Weibull distribution plot of ln(ln(1/(1-F))) vs ln (σ) for the four fibre shapes is shown in Fig. 11. Although there is a large disparity among the fibres, on average, the data points and fitting curves have shown a good agreement [32]. The slope of the Weibull diagram, m, influences the fibre strength's peak value, as a small modulus results in a wide range of fibre strength values.
Table 2 presents a summary of the Weibull modulus, characteristic strength, and the coefficient of determinant (R-Square) values. HMS fibres have the highest Weibull modulus, indicating that their failure strength is more predictable than that of other fibre shapes. ITS fibres, on the other hand, have the lowest Weibull modulus showing that the strength of these fibres may be predicted using a wide range probability curve and this results in a low probability of prediction. The EOS curves show a good deal of agreement between the data points and the fitting curve, showing that Weibull statistics will predict their failure quite well. For all fibre shapes except EOS, the R-squared value is similar, indicating that the tensile strength distribution of these fibres has a similar linear

regression approximation in the Weibull diagram.

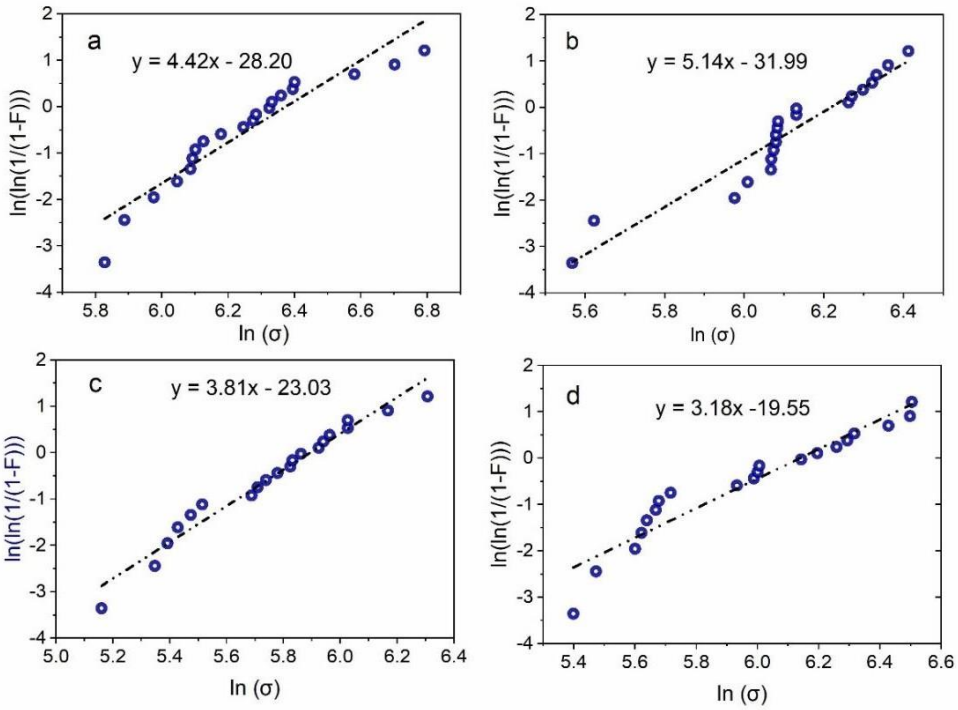

Fig. 11. Weibull distribution for the tensile strength of different fibre shapes; a) COS fibres, b) HMS fibres, c) EOS fibres, and d) ITS fibres.

Table 2

The Weibull modulus and the characteristic strength of the enset fibres of different geometry

Fibres	Number of Observations	Weibull Modulus, m	Characteristic Strength, σ_0 (MPa)	R-Square
HMS	20	5.14	504.58	0.91
COS	20	4.42	589.98	0.90
ITS	20	3.18	467.69	0.91
EOS	20	3.91	361.41	0.97

The Weibull statistics for these fibres are evaluated based on the volume variation due to fibre cross-section. The effect of test length-based volume variation is not included in the framework of this study (the authors are working on it and the outputs will be reported to in another paper). The Weibull evaluation showed that the volume of the fibres is not a significant parameter to consider for the various fibre geometry. Based on the Weibull assumption, the EOS fibre, which has the smallest diameter, would be projected to have the highest strength. It does, however, deliver the least amount of strength. The second-highest property is provided by the largest fibre, HMS, which

would be projected to have the lowest strength value. As a result, a Weibull analysis including consideration of a volume effect is not proper for the evaluated enset fibres.

3.6. Contribution to composite strength

The contribution of fibres of different geometry when they are bundled together in a composite was investigated. This was accomplished by investigating the load-carrying proportion and the failure properties of the various fibres by considering their average tensile strength value. As discussed in section 3.2, four fibre geometries have been identified in enset fibre and additionally, small fibres have been classified as one fibre family not because of their geometry but due to their size.

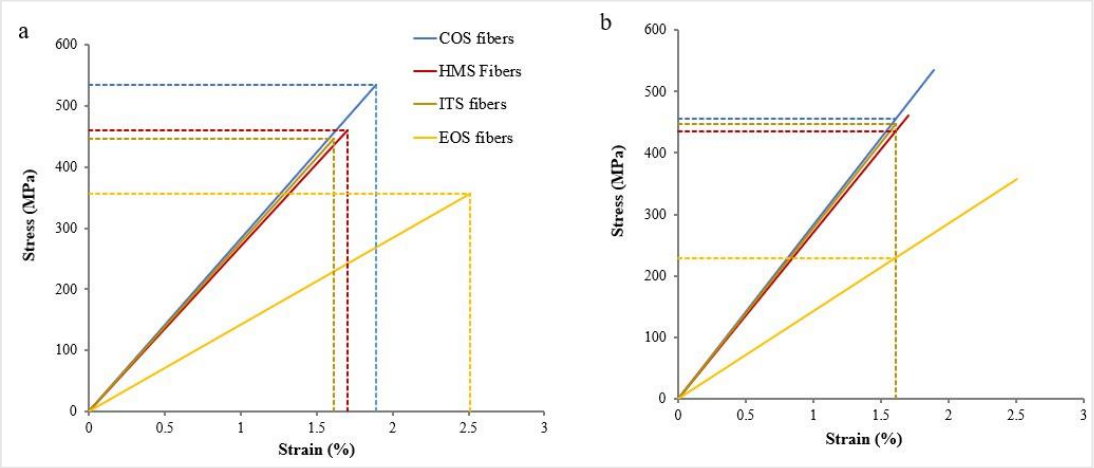

Fig. 12. a) Stress-strain maps of the various fibre shapes, and b) their stress contribution to the composite stress at the strain to failure value of ITS fibres.

However, the geometry of these fibres resembles on average a circular shape as they are formed with small numbers of elementary fibres that possess nearly a circular shape. Moreover, these fibres are small in cross-section which means that they can be expected to provide relatively high tensile strength. Therefore, it is considered reasonable to group these fibres with the COS fibres. The stress-strain curve of various fibre types is shown in Fig. 12 (a). Because these fibres have varied strengths and strain to failure values, they are expected to contribute differently to the global tensile behaviour of enset fibre reinforced composite structures. The strain-to-failure values show that fibres with intricate shapes fail first, followed by HMS fibres.

Cognizant of the assumption that the fibres are distributed randomly, ITS fibres are expected to initiate the first cracks at multiple points, create local stress concentrations, and may be assumed to all fail at this stage. The whole failure of the bundle, however, may not be seen while the ITS fibres

begin to fail due to the minor areal contribution compared to other geometric fibres. The fibre which decides the final failure of the composite can be obtained using the composite's back-calculated strength value [46]. As a result of the strain to failure value, the composite structure may have two failure stages: Failure of the ITS fibres in stage one, and subsequent failure of the next least ductile HMS shape fibres in stage two. In stage 1, the intricate form fibres begin to fail, and the load-carrying distribution of all fibres is equal to their average Young's modulus (assuming a linear stress-strain behaviour) times the failure strain of the first failing ITS fibres. The stress-strain map of the various fibres, as well as their relative stress values at the ITS strain to failure value, are shown in Fig. 12b. As a result, the stress share of the various fibres is computed from their respective stress value and area contribution in the fibre bundle.

Table 2 shows how the contribution of the various fibre types to the predicted technical fibre bundle strength was calculated. Because of this, while COS fibres have a high contribution at the fibre level because of their high Young's modulus, HMS fibres have the highest contribution at the bundle level due to their high areal contribution. The analysis in Table 3 predicts a total stress uptake potential of the fibre bundle of 415 MPa. When the fibre volume fraction of 48% is considered, this would result in a composite strength of 199 MPa.

Table 3

Contribution of the typical fibre shapes to the tensile load at the strain to failure value of ITS fibres

Fibre Geom.	Areal Cont. (%)	ε (%)	σ (MPa)	slope	ε@ITS	stress	Instant Load	Load Cont. (%)
				Δσ/Δε	%	slope*ε @ITS	Areal cont. (%) *σ	
COS	33	1.89	534.52	282.81	1.61	455.32	150.26	36
HMS	44	1.7	460.42	270.84	1.61	436.05	191.86	46
ITS	13	1.61	410.01	254.66	1.61	410	53.3	13
EOS	10	2.8	332.16	118.63	1.61	190.99	19.1	5

When investigating the technical fibre properties, from the IFBT test results, the back-calculated average technical fibre strength is 339.20 ±29.43 MPa. This shows that the composite fails earlier than predicted from the contribution of the various fibre types (415 MPa). This may be due to local stress concentrations leading to premature composite failure. This also means that a potential second stage of behaviour, post failure of the ITS fibres, does not need to be considered.

3.7. Failure properties of fibre shapes

The areas of fibre failure were examined to study the physical phenomena that occur when fibres break. The failure phenomena were evaluated at both composite and fibre levels. Figure 13a shows microscopic images of the tensile failure region of the composite samples obtained by SEM. The failure profile shows that fibre pull-out phenomena occurred in reinforcing fibres. Fibre pullout is more pronounced in HMS and COS fibres than in EOS and ITS fibres. In addition, the variation in failure profile varies between fibre shapes and within the fibre itself. Unlike other fibre forms, COS fibres show a less noticeable variation in intra-fibre failure profile. On the other hand, HMS fibres hold two distinct failure zones, which are often separated in the middle (Figure 13b). One of the most probable reasons is the presence of elementary fibres with disproportionate lumen sizes in the centre of the fibre. This weakens and divides the technical fibre into two semi-symmetrical sections that can act independently of each other during loading.

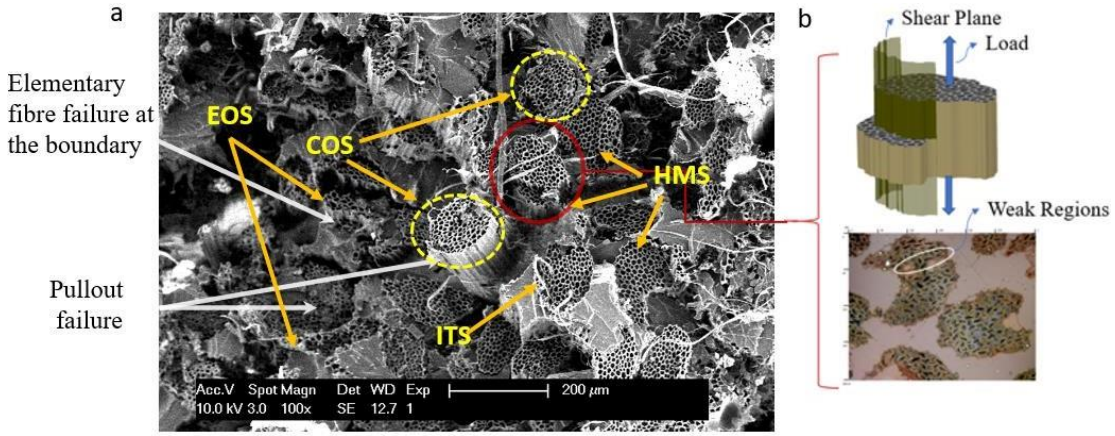

Fig. 13. SEM micrograph of the failure surface of the composite showing a) an overview of various fibres, b) a schematic of the failure of a typical HMS technical fibre, and the weak region

Furthermore, fibre splitting has been seen within the HMS technical fibre. This shows the interface strength between the elementary fibres is locally weaker than the fibre's interface with the epoxy matrix. This fibre splitting behaviour also means these fibres can own low tensile properties in the transverse direction. Moreover, fibres in the HMS category also show a more complex failure mode than the two-region type. This was seen from those that have nearly uniform lumen size distribution across the fibre structure.

The fibre level failure profile of the various fibre shapes during single fibre testing is presented in

Fig. 14. COS fibres experience a failure behaviour similar to that at the composite level (Fig. 14a). Unlike other fibre shapes, the elementary fibres on the edge and inner part of the technical fibre have a plain failure. This suggests almost equivalent stress distribution is exerted in the bundle of elementary fibres due to the smallest perimeter-to-area ratio. This predominantly leads to elementary fibres' separation due to central lamella defects [32].

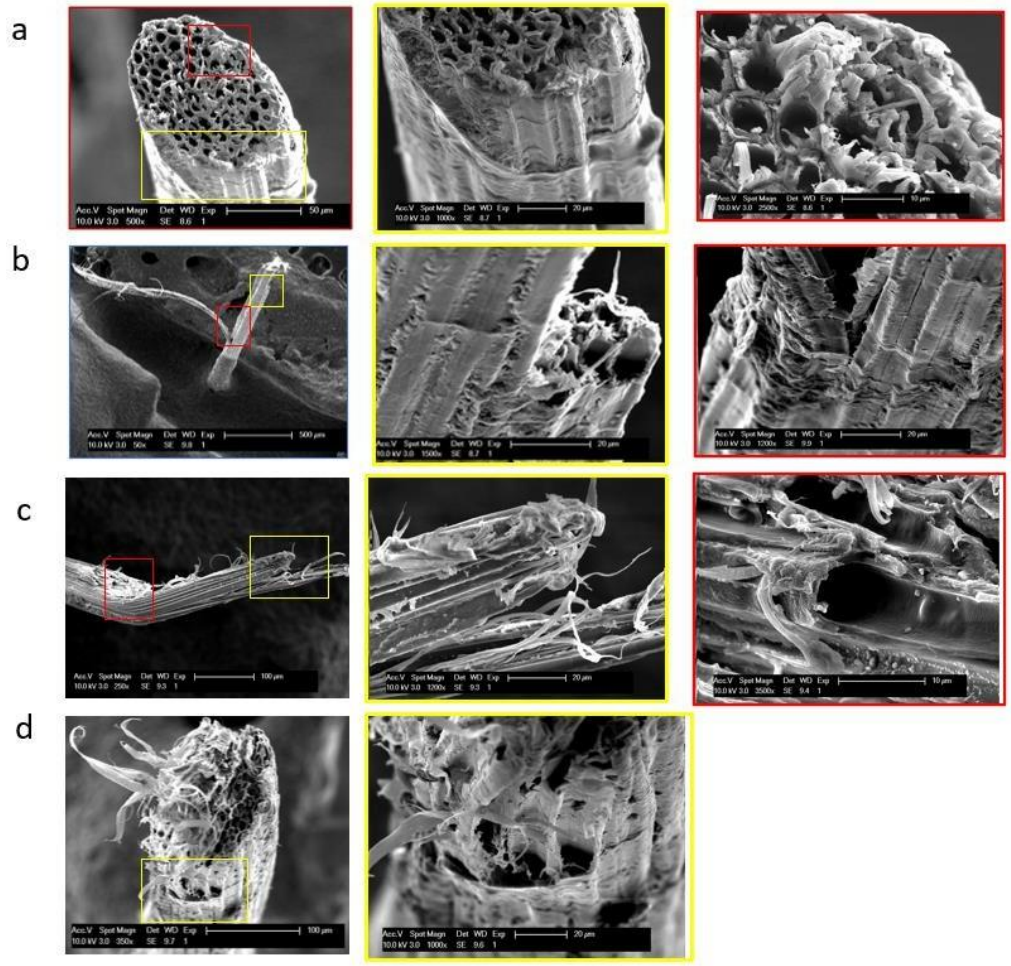

Fig. 14. SEM microstructural images of failure area of various fibre shapes; a) COS fibres, b) HMS fibres, c) EOS fibres and d) ITS fibres, during single fibre testing

The HMS fibres experienced fibre splitting and a semi-symmetric failure profile similar to the failure pattern observed at the composite level (Fig. 14b). This splitting is evenly distributed across the cross-sectional area of the technical fibre. It is observed over a long range of the fibre length, indicating that the weak link in these fibre shapes is an intrinsic behaviour along the fibre axis.

The EOS fibres experience fibrillation, and fibre failure begins randomly along the bundle of

elementary fibres (Fig. 14c). This phenomenon is not equally seen at the composite level, likely because the matrix repairs and restrains the fibres from experiencing fibrillation. However, regardless of the extent, the difference in the failure profile of the elementary fibres at the centre and edge of the technical fibre appears at the fibre and composite levels. Therefore, more fibrillations occur in the single fibre test due to more elementary fibres being exposed to the environment, and the central lamella is not capable enough to evenly transfer the stress. On the other hand, ITS fibres have shown variations in failure profile at the edge and inside the fibre. The elementary fibres at the boundary of the fibre cross-section have different failure topography than those inside the fibre (Fig. 14d). These fibres have similar failure profiles at the composite and fibre levels.

4. Conclusions

This study investigates the geometric appearance of enset fibres, their probability of occurrence and area contribution, their tensile properties, and their contribution to the global unidirectional tensile load on the fibre bundles. Four basic geometric shapes have been identified; namely half-moon shape, circular/oval shape, elongated shape, and intricate shape fibres. A generic equation has been devised to represent these diverse shapes of fibres, with the model's parameters obtained from micrographs using powerful image processing tools like MATLAB. Moreover, fibres that are small due to containing a small number of elementary fibres, are grouped as small shape fibres, modelled with circular fitting. In the enset fibre population taken from four large-size microscopic images, which accounts for about 1822 fibres, while small fibres occurred dominantly, half-moon fibres accounted for the largest areal contribution.

Fibres with various geometries exhibited varying tensile properties, including strength, Young's modulus, and strain to failure. Circular or oval-shaped fibres demonstrated the highest tensile properties compared to other fibre types, followed by half-moon shaped fibres. The Weibull analysis indicates that the strength of the fibres is not affected by their volume as attributed to changes in diameter. However, it is recognised that the strength and elastic modulus of enset fibres are significantly influenced by their geometric properties, particularly the perimeter-to-area ratio. This ratio measures the proportion of elementary fibres at the boundary compared to those completely enclosed within the technical fibre.

Due to the uneven contribution of the elementary fibres at the boundary and inside the engineering fibre to the total stress and elastic modulus, fibres with a large perimeter-to-area ratio have lower tensile strength and elastic modulus and vice versa. This disparity is attributed to the vulnerability of the elementary fibres at the boundary to asymmetric loading under tension, resulting in relatively stress-free elongation and overall weaker structural integrity. In contrast, fibres with a small circumference-to-area ratio experience predominantly symmetrical loading on the elementary fibres, resulting in a more uniform stress distribution throughout the structure. This results in an increase in the strength and elastic modulus of the fibres compared to those with a large perimeter-to-area ratio.

The investigation on the load contribution of the various fibres illustrated that half-moon fibres provide the largest contribution to the global tensile load due to their highest share of the areal contribution. It is noted that the intricate shapes are the first fibres to break due to their low strain-to-failure value. Because the calculated stress level for their failure, is higher than the observed bundle tensile strength, apparently when some of the ITS fibres fail, the entire composite starts to fail, likely due to stress concentrations. Unlike the other fibre types, the half-moon-shaped fibres exhibited two different failure regions because of a weak region at the centre caused by the disproportionate lumen size of the elementary fibres. This weak region leads the fibres to experience fibre splitting and pull-out failure modes when subjected to tension. This failure behaviour has been observed both at the fibre and composite levels. On the other hand, COS fibres have a nearly uniform failure profile. The EOS fibres experience fibrillation in single fibre test breaks; however, this failure profile is not evident at the composite level as the polymer matrix constrains such failures. In the ITS, the failure profile at the composite and fibre levels is similar. The elementary fibres at the boundary have different failure topography than those inside the technical fibres.

Acknowledgements

This research work was carried out in the frame of the IUPEPPE project (International University Partnership Services for the Establishment of Postgraduate Programmes in Ethiopia) funded through GIZ GmbH and the International University Partnership for the Establishment of PhD Programmes in Ethiopia funded by the Ethiopian Ministry of Science and Higher Education.

References

[1] Praveena BA, Buradi A, Santhosh N, Vasu VK, Hatgundi J, Huliya D. Study on characterization of mechanical, thermal properties, machinability and biodegradability of natural fiber reinforced polymer composites and its Applications, recent developments and future potentials: A comprehensive review. Mater Today Proc, vol. 52, Elsevier Ltd; 2022, p. 1255–9. https://doi.org/10.1016/j.matpr.2021.11.049.

[2] Bensadoun F, Vanderfeesten B, Verpoest I, Van Vuure AW, Van Acker K. Environmental impact assessment of end of life options for flax-MAPP composites. Ind Crops Prod 2016;94:327–41. https://doi.org/10.1016/j.indcrop.2016.09.006.

[3] Abidin NIZ, Sabri MFM, Kalantari K, Afifi AM, Ahmad R. Corrosion detection for natural/synthetic/textiles fiber polymer composites. Structural Health Monitoring of Biocomposites, Fibre-Reinforced Composites and Hybrid Composites, Elsevier; 2018, p. 93–112. https://doi.org/10.1016/B978-0-08-102291-7.00006-X.

[4] Hybrid-Biocomposite Material for Corrosion Prevention in Pipeline a review n.d.

[5] Wang X, Petrů M, Yu H. The effect of surface treatment on the creep behavior of flax fiber
reinforced composites under hygrothermal aging conditions. Constr Build Mater 2019;208:220–7. https://doi.org/10.1016/j.conbuildmat.2019.03.001.

[6] Misra M, Ahankari SS, Mohanty AK, Nga AD. 11 - Creep and fatigue of natural fibre composites. In: Zafeiropoulos NE, editor. Interface Engineering of Natural Fibre Composites for Maximum Performance, Woodhead Publishing; 2011, p. 289–340. https://doi.org/https://doi.org/10.1533/9780857092281.2.289.

[7] Wambua P, Ivens J, Verpoest I. Natural fibres: Can they replace glass in fibre reinforced plastics? Compos Sci Technol 2003;63:1259–64. https://doi.org/10.1016/S0266-3538(03)00096-4.

[8] Amada S, Ichikawa Y, Munekata T, Nagase Y, Shimizu H. Fiber texture and mechanical graded structure of bamboo. vol. 28. 1997.

[9] Garat W, Corn S, Le Moigne N, Beaugrand J, Bergeret A. Analysis of the morphometric variations in natural fibres by automated laser scanning: Towards an efficient and reliable assessment of the cross-sectional area. Compos Part A Appl Sci Manuf 2018;108:114–23. https://doi.org/10.1016/j.compositesa.2018.02.018.

[10] Li Y, Mai Y-W, Ye L. Sisal ®bre and its composites: a review of recent developments. n.d.

[11] Tran LQN, Minh TN, Fuentes CA, Chi TT, Van Vuure AW, Verpoest I. Investigation of microstructure and tensile properties of porous natural coir fibre for use in composite materials. Ind Crops Prod 2015;65:437–45. https://doi.org/10.1016/j.indcrop.2014.10.064.

[12] Hamad SF, Stehling N, Holland C, Foreman JP, Rodenburg C. Low-Voltage SEM of Natural Plant Fibers: Microstructure Properties (Surface and Cross-Section) and their Link to the Tensile Properties. Procedia Eng, vol. 200, Elsevier Ltd; 2017, p. 295–302. https://doi.org/10.1016/j.proeng.2017.07.042.

[13] Das SC, La Rosa AD, Goutianos S, Grammatikos SA. Flax fibers, their composites and application. Plant Fibers, their Composites, and Applications, Elsevier; 2022, p. 209–32. https://doi.org/10.1016/b978-0-12-824528-6.00017-5.

[14] Baley C, Gomina M, Breard J, Bourmaud A, Davies P. Variability of mechanical properties of flax fibres for composite reinforcement. A review. Ind Crops Prod 2020;145. https://doi.org/10.1016/j.indcrop.2019.111984.

[15] Depuydt DEC, Sweygers N, Appels L, Ivens J, van Vuure AW. Bamboo fibres sourced from three global locations: A microstructural, mechanical and chemical composition study. Journal of

Reinforced Plastics and Composites 2019;38:397–412. https://doi.org/10.1177/0731684419828532.

[16] Wang H, An X, Li W, Wang H, Yu Y. Variation of mechanical properties of single bamboo fibers (Dendrocalamus latiflorus Munro) with respect to age and location in culms 2014;68:291–7. https://doi.org/doi:10.1515/hf-2013-0081.

[17] Depuydt DEC, Billington L, Fuentes C, Sweygers N, Dupont C, Appels L, et al. European bamboo fibres for composites applications, study on the seasonal influence. Ind Crops Prod 2019;133:304–16. https://doi.org/10.1016/j.indcrop.2019.03.026.

[18] Thomason JL. Flat glass fibres: The influence of fibre cross section shape on composite micromechanics and composite strength. Compos Part A Appl Sci Manuf 2023;169. https://doi.org/10.1016/j.compositesa.2023.107503.

[19] Kitagawa Y, Yoshimura A, Arai M, Goto K, Sugiura N. Experimental and numerical evaluation of effects of kidney-shape carbon fiber on transverse cracking of carbon fiber reinforced plastics. Compos Part A Appl Sci Manuf 2022;152. https://doi.org/10.1016/j.compositesa.2021.106690.

[20] Liu X, Wang R, Wu Z, Liu W. The effect of triangle-shape carbon fiber on the flexural properties of the carbon fiber reinforced plastics. Mater Lett 2012;73:21–3. https://doi.org/10.1016/j.matlet.2012.01.003.

[21] Park SJ, Seo MK, Shim HB. Effect of fiber shapes on physical characteristics of non-circular carbon fibers-reinforced composites. Materials Science and Engineering: A 2003;352:34–9. https://doi.org/10.1016/S0921-5093(02)00463-X.

[22] Thomason J. The Influence of Fibre Cross Section Shape and Fibre Surface Roughness on Composite Micromechanics. Micro 2023;3:353–68. https://doi.org/10.3390/micro3010024.

[23] Garat W, Corn S, Le Moigne N, Beaugrand J, Bergeret A. Analysis of the morphometric variations in natural fibres by automated laser scanning: Towards an efficient and reliable assessment of the cross-sectional area. Compos Part A Appl Sci Manuf 2018;108:114–23. https://doi.org/https://doi.org/10.1016/j.compositesa.2018.02.018.

[24] Ntenga R, Beakou A. Structure, morphology and mechanical properties of Rhectophyllum camerunense (RC) plant-fiber. Part I: Statistical description and image-based reconstruction of the cross-section. Comput Mater Sci, vol. 50, 2011, p. 1442–9. https://doi.org/10.1016/j.commatsci.2010.11.032.

[25] Nurfeta A, Tolera A, Eik LO, Sundstøl F. The supplementary value of different parts of enset (Ensete ventricosum) to sheep fed wheat straw and Desmodium intortum hay. Livest Sci 2008;119:22–30. https://doi.org/10.1016/j.livsci.2008.02.010.

[26] Lemawork S, Azerefegne F, Alemu T, Addis T, Blomme G. Evaluation of entomopathogenic fungi against Cataenococcus ensete [Williams and Matile-Ferrero, (Homoptera: Pseudococcidae)] on enset. Crop Protection 2011;30:401–4. https://doi.org/10.1016/j.cropro.2010.12.018.

[27] Herak D. Mechanical behaviour of polymeric composite with fibres of false banana (Ensete ventricosum). n.d.

[28] Bensadoun F, Verpoest I, Baets J, Müssig J, Graupner N, Davies P, et al. Impregnated fibre bundle test for natural fibres used in composites. Journal of Reinforced Plastics and Composites 2017;36:942–57. https://doi.org/10.1177/0731684417695461.

[29] Greenspan L. Humidity Fixed Points of Binary Saturated Aqueous Solutions. vol. 81. 1976.

[30] Weibull Distri 3. Weibull Distributions and Their Applications. n.d.

[31] Benjeddou O. Weibull statistical analysis and experimental investigation of size effects on tensile behavior of dry unidirectional carbon fiber sheets. Polym Test 2020;86. https://doi.org/10.1016/j.polymertesting.2020.106498.

[32] Defoirdt N, Biswas S, Vriese L De, Tran LQN, Acker J Van, Ahsan Q, et al. Assessment of the tensile properties of coir, bamboo and jute fibre. Compos Part A Appl Sci Manuf 2010; 41:588–95. https://doi.org/https://doi.org/10.1016/j.compositesa.2010.01.005.

[33] Trujillo E, Moesen ML, Van Vuure A, Ivens J, Verpoest I. ECCM15-15 TH EUROPEAN CONFERENCE Weibull statistics of bamboo fibre bundles: methodology for tensile testing of natural fibres. n.d.

[34] Trujillo E, Moesen M, Osorio L, Van Vuure AW, Ivens J, Verpoest I. Bamboo fibres for reinforcement in composite materials: Strength Weibull analysis. Compos Part A Appl Sci Manuf 2014;61:115–25. https://doi.org/10.1016/j.compositesa.2014.02.003.

[35] Langhorst A, Ravandi M, Mielewski D, Banu M. Technical agave fiber tensile performance: The effects of fiber heat-treatment. Ind Crops Prod 2021;171. https://doi.org/10.1016/j.indcrop.2021.113832.

[36] Acitas S, Aladag CH, Senoglu B. A new approach for estimating the parameters of Weibull distribution via particle swarm optimization: An application to the strengths of glass fibre data. Reliab Eng Syst Saf 2019;183:116–27. https://doi.org/10.1016/j.ress.2018.07.024.

[37] Zhang LF, Xie M, Tang LC. A study of two estimation approaches for parameters of Weibull distribution based on WPP. Reliab Eng Syst Saf 2007;92:360–8. https://doi.org/10.1016/j.ress.2006.04.008.

[38] Nakka R, Harursampath D, Pathan M, Ponnusami SA. A computationally efficient approach for generating RVEs of various inclusion/fibre shapes. Compos Struct 2022;291. https://doi.org/10.1016/j.compstruct.2022.115560.

[39] Davoodi Kermani I, Schmitter M, Eichinger JF, Aydin RC, Cyron CJ. Computational study of the geometric properties governing the linear mechanical behavior of fiber networks. Comput Mater Sci 2021;199. https://doi.org/10.1016/j.commatsci.2021.110711.

[40] Amroune S, Belaadi A, Bourchak M, Makhlouf A, Satha H. Statistical and Experimental Analysis of the Mechanical Properties of Flax Fibers. Journal of Natural Fibers 2022;19:1387–401. https://doi.org/10.1080/15440478.2020.1775751.

[41] Aslan M, Chinga-Carrasco G, Sørensen BF, Madsen B. Strength variability of single flax fibres. J Mater Sci, vol. 46, 2011, p. 6344–54. https://doi.org/10.1007/s10853-011-5581-x.

[42] Mesquita F, Bucknell S, Leray Y, Lomov S V., Swolfs Y. Single carbon and glass fibre properties characterised using large data sets obtained through automated single fibre tensile testing. Compos Part A Appl Sci Manuf 2021;145. https://doi.org/10.1016/j.compositesa.2021.106389.

[43] Ansell MP, Mwaikambo LY. The structure of cotton and other plant fibres. Handbook of Textile Fibre Structure, vol. 2, Elsevier Inc.; 2009, p. 62–94. https://doi.org/10.1533/9781845697310.1.62.

[44] Nian G, Li Q, Xu Q, Qu S. A cohesive zone model incorporating a Coulomb friction law for fiber-reinforced composites. Compos Sci Technol 2018;157:195–201. https://doi.org/10.1016/j.compscitech.2018.01.037.

[45] Andrianov I V., Danishevs'Kyy V V., Weichert D. Boundary layers in fibrous composite materials. Acta Mech 2011;216:3–15. https://doi.org/10.1007/s00707-010-0333-6.

[46] Prapavesis A, Tojaga V, Östlund S, Willem van Vuure A. Back calculated compressive properties of flax fibers utilizing the Impregnated Fiber Bundle Test (IFBT). Compos Part A Appl Sci Manuf 2020;135. https://doi.org/10.1016/j.compositesa.2020.105930.